ACS APPLIED MATERIALS & INTERFACES

Research Article

www.acsami.org

Novel and Facile Method, Dynamic Self-Assemble, To Prepare SnO_2/rGO Droplet Aerogel with Complex Morphologies and Their Application in Supercapacitors

Mingxi Chen,[†] Huan Wang,[†] Lingzhi Li,[†] Zhe Zhang,[†] Cong Wang,[†] Yu Liu,*[,†,‡] Wei Wang,[§] and Jianping Gao*[,†,‡]

[†]School of Science, Tianjin University, Tianjin 300072, People's Republic of China

[‡]Collaborative Innovation Center of Chemical Science and Engineering, Tianjin 300072, People's Republic of China

[§]School of Chemical Engineering, Tianjin University, Tianjin 300072, People's Republic of China

Supporting Information

ABSTRACT: A facile and novel method to prepare SnO_2/reduced graphene oxide (rGO) droplet aerogels with complex morphologies had been developed. This method has been named dynamic self-assemble. Aerogels with both "egg-tart" and "mushroom" shapes were obtained by this method. The changes in the graphene oxide (GO) droplet morphologies during the dynamic process of a GO droplet falling into a $SnCl_2$ target solution were monitored using a high speed camera. The formed SnO_2/rGO aerogels were then characterized by Raman spectroscopy, thermogravimetric analysis, X-ray diffraction analysis, and X-ray photoelectron spectroscopy. The microstructures of the SnO_2/rGO aerogels were observed with scanning electron microscopy and transmission electron microscopy. Finally, the SnO_2/rGO droplet aerogels were used as the electrode material in a symmetrical two-electrode supercapacitor and the electrochemical performance of the supercapacitor was investigated using cyclic voltammetry and galvanostatic charge/discharge methods. The SnO_2/rGO electrodes demonstrated excellent electrochemical performance and stability. At a scan rate of 5 mV/s, their highest gravimetric and volumetric specific capacitances were 310 F/g and 180 F/cm^3, respectively, and their energy and power densities were as high as 30 Wh·kg^{-1} and 8.3 kW·kg^{-1}, respectively.

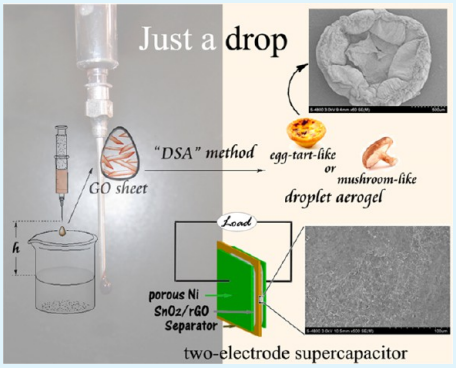

KEYWORDS: *SnO_2 nanoparticles, graphene aerogel, dynamic self-assemble, complex morphologies, supercapacitor*

1. INTRODUCTION

Tin dioxide is a traditional semiconductor material that has been actively researched over the last two decades. This is because of its shape- and size-dependent physical, chemical, electronic, optical, and catalytic properties.[1,2] It has wide applications in lithium-ion batteries,[3] gas sensors,[4] sensitized solar cells,[5] and catalysts.[6] SnO_2 has been considered to be one of the most promising anode materials for high performance lithium-ion batteries;[1,7] however, using it in supercapacitors has only just begun in the past few years. Recently, Liu and co-workers reported on a hydrothermal synthesis of hierarchical SnO_2 nanostructures, which gave rise to the specific capacitance of 187.7 F·g^{-1} at current densities of 1.0 A·g^{-1}.[8] Wang et al. prepared SnO_2/graphene using a microwave-assisted one-pot synthesis, which showed a specific capacitance of 99.7 F/g.[9] On the basis of these findings, more investigations can be done to improve the specific capacitance of SnO_2-based materials to meet the criteria for excellent supercapacitors.

Since it was first reported by Novoselov and co-workers in 2004, graphene has received widespread attention.[10,11] Owing to its remarkable chemical, mechanical, and electronic properties, it has great potential for applications in a variety of fields including photonic and electronic devices, energy, the environment, chemical engineering, materials science, and biotechnology.[12−14] Current methods to prepare graphene and graphene-like materials include the micromechanical exfoliation of graphite,[10] chemical vapor deposition,[15] epitaxial growth,[16] and the chemical reduction of graphene oxide (GO).[17] The most promising and economically viable approach for the large-scale production of graphene-based materials is the chemical reduction of graphene oxide, in which cheap graphite powder is first oxidized using a strong oxidant to produce exfoliated GO and then the graphene oxide is reduced by chemical reduction or other routes.[18] Importantly, GO is versatile, dispersible in water, and easy to modify, which makes it easy to process and use. For instance, the extraordinarily high surface areas of GO and its derivatives make it an important catalyst support for metals, metal oxides, and enzyme catalysts.[19−21] These

Received: June 8, 2014
Accepted: August 1, 2014
Published: August 1, 2014

supported catalysts can have enhanced chemical-, electrochemical-, and photocatalytic activities.[19,22]

Graphene tends to assemble into a sponge-like material known as an aerogel during chemical reduction or during hydrothermal treatment.[23,24] Aerogels have extremely low densities and high porosities and thus are conducive for increasing catalytic loads and the number of active sites in catalysts. They therefore have extensive applications in the fields of energy and the environment and can be used for things like ion or organic solvent absorption or energy storage.[25] Because the profuse interlayer structures exist between the layers of graphene aerogel, it exhibited both high electrical conductivity and large surface area.[26] Therefore, graphene aerogel can be used as electrode materials directly without addition of a binder and conductive agent. However, currently these reduced graphene oxide (rGO) aerogels are all prepared under static conditions.[23−27] The preparation of graphene aerogels under dynamic conditions has not been reported.

The impact of a droplet onto the surface of a liquid pool is a dynamic process and several different collision dynamics, such as floating, total or partial coalescence, jetting, bouncing, and splashing, can be observed.[28,29] Such phenomena depend on various parameters, which include the physical and chemical properties of the liquids, the depth of the liquid reservoir, and, most importantly, the impact velocity of the drop.[30,31] Although, the phenomenon of the partial coalescence of a droplet was first reported almost 50 years ago,[32] with the advent of fast cameras and powerful numerical simulations, it has recently again received considerable attention,[31,33] There are fascinating morphology changes which can be observed at the moment that a falling droplet impacts a reservoir of fluid.[33] These changes in morphology offer a way to prepare particles with nonregular shapes.

In this work, a SnO_2/rGO droplet aerogel was prepared by a "dynamic self-assembly" (DSA) method at room temperature. When a GO droplet impacted the surface of a $SnCl_2$ solution, GO sheets were reduced by the Sn^{2+} ions and they simultaneously assembled into a three-dimensional hydrogel. More interestingly, the morphology of the SnO_2/rGO hydrogel changed, owing to partial coalescence, and "egg-tart-like" and "mushroom-like" shapes were obtained with sufficiently controlling the falling height (h) of the droplets onto the $SnCl_2$ solution and the diameter of the needles. The dried SnO_2/rGO droplet hydrogels (SnO_2/rGO droplet aerogels) were characterized and tested as the electrode material in supercapacitors of two-electrode systems.

2. EXPERIMENTAL SECTION

2.1. Materials. Graphite was obtained from Qingdao Graphite Factory. Tin(II) chloride dihydrate and methylthionine chloride were purchased from Aladdin Industrial Co. Potassium permanganate, sodium nitrate, concentrated sulfuric acid, 30% hydrogen peroxide, hydrochloric acid, ethanol, nickel foam, and all other reagents were all purchased from Tianjin Chemical Reagent Co. All the chemicals were analytical grade and used as received.

2.2. Self-Assembly of SnO_2/rGO Droplet Aerogels. Graphene oxide was prepared by a modified Hummer's method.[34] The GO sheets were then suspended in water with a concentration of 10 mg·mL^{-1}.

Different concentrations of $SnCl_2$ solutions were prepared by dissolving $SnCl_2$ powder in distilled water and then adding a small amount of HCl to inhibit the hydrolysis of the Sn^{2+} ions. Next, the GO suspension (10 g/L) was placed in a syringe with a stainless steel needle and drops of the suspension were allowed to fall under their own weight from the needle. A high speed camera (Fastcam Super 10KC, PHO-TRON, Japan,) with a maximum frame rate of 1000 Hz was used to record the reaction of the GO droplet and the $SnCl_2$ solution.

The effect of the distance (10 to 100 mm) between the tip of the needle and the surface of the reservoir (volume 100 mL, height of 50 mm), the outer diameters of the needle (0.45, 1.6, and 8 mm) on the morphology of the formed product were investigated.

After the GO droplets were added to the $SnCl_2$ solution, the mixture was allowed to stand at room temperature for 4 h, so that all reactions within the system had time to go to completion. Finally, the product was transferred into a hermetic vessel filled with distilled water and shaken on the multifunction shaker (WH-4, Weihua Instruments, Inc.) to remove any excess chloride ions. The products were freeze-dried for 48 h to remove the water to obtain SnO_2/rGO aerogels. The concentration of $SnCl_2$ solution was varied and the resultant SnO_2/rGO droplet aerogels are designated as SnO_2/rGO-80 or SnO_2/rGO-20 for $SnCl_2$ solution concentrations of 80 and 20 g/L, respectively.

2.3. Characterization. *2.3.1. Scanning Electron Microscopy (SEM).* The SnO_2/rGO aerogels were coated with gold using a sputter coater (Desk-II; Denton Vacuum), and then their morphologies were observed with a scanning electron microscope (S-4800, Thermo).

2.3.2. Transmission Electron Microscopy. The samples for transmission electron microscopy (TEM) observation were prepared by placing drops of the diluted SnO_2/rGO aqueous suspension onto a carbon coated copper grid, which was then dried under ambient conditions prior to being introduced into the TEM chamber. TEM observation and energy dispersive X-ray spectroscopy (EDS) were performed using a Philips Tecnai G2F20 microscope at 200 kV.

2.3.3. Raman Microscopy Analysis. Raman measurements were performed with a high resolution Raman Microscope (Renishaw, U.K.) in a backscattering configuration.

2.3.4. X-ray Diffraction Analysis. The X-ray diffraction (XRD) spectra of the samples were measured using an X-ray diffractometer (D/MAX-2500, Rigaku Corporation, Japan) with reference target: Cu Kα radiation (λ = 1.54 Å); voltage, 40 kV; current, 100 mA. The samples were measured from 10° to 90° (2θ) with steps of 4° min^{-1}.

2.3.5. Thermogravimetric Analysis. The samples were first dried in a vacuum at 40 °C for 2 days before the thermogravimetric curves (TGA) were recorded with a Rigaku-TD-TDA analyzer at a heating rate of 10 °C/min.

2.3.6. X-ray Photoelectron Spectroscopy (XPS) Analysis. The elemental composition of the SnO_2/rGO aerogels was analyzed using an X-ray photoelectron spectrometer with an Mg Kα anode (PHI1600 ESCA System, PerkinElmer, U.S.).

2.3.7. N_2 Adsorption and Desorption Isotherms. Nitrogen adsorption and desorption isotherms of SnO_2/rGO powders were measured at 77 K using an AUTOSORB iQ instrument (Quantachrome, U.S.). The total surface area was calculated from the Brunauer−Emmett−Teller (BET) method and the pore size distribution data was calculated using the density functional theory (DFT) method based on the adsorption and desorption data.

2.4. Two-Electrode Electrochemical Testing. The SnO_2/rGO droplet aerogel (after weighing, prepared with the 8 mm needle) was pressed onto pieces of porous nickel (as current collectors), and then used as electrodes in the symmetrical supercapacitor. The above electrodes separated by a porous separator (AS-CN1) were immersed in 2.0 M KOH solution for 12 h. The supercapacitor was assembled in a symmetrical two-electrode configuration, namely, as a test cell consisting of two electrodes (containing porous nickel as current collectors) and a porous separator supported in a test fixture consisting of two Teflon plates. All electrochemical characterizations of the symmetrical two-electrode system were performed with an electrochemical workstation (CH Instruments, Inc., Shanghai) using a 2.0 M potassium hydroxide solution as the electrolyte.

The gravimetric and volumetric specific capacitances, C_{s-M} ($F{\cdot}g^{-1}$) and C_{s-V} ($F{\cdot}cm^{-3}$), respectively, for a single electrode were calculated from the galvanostatic charge−discharge curves according to the equation:

$$C_{s-M} = \frac{4I}{m \cdot \Delta V/\Delta t} C_{s-V} = \frac{4I}{V \cdot \Delta V/\Delta t}$$

where I is the current (which is constant), m and V are the total mass and total volume for both carbon electrodes, respectively, and $\Delta V/\Delta t$ was calculated from the slope of the line fitted to the discharge curve over the range V_{max} to (1/2) V_{max}.

The energy densities, E (Wh·kg^{-1}), were normalized to the mass of the two carbon electrodes and the total volume of the cell and was estimated using the following equation:

$$E = \frac{1}{2} CV^2$$

The power densities, P_M (W·kg^{-1}), were calculated using

$$P_M = \frac{\Delta V^2}{4R_{ESR}m}$$

3. RESULT AND DISCUSSION

3.1. Formation of SnO_2/rGO Droplet Aerogels by Dynamic Self-Assembly Method. Studies on the dynamic processes of the partial coalescence between droplets and a target liquid have demonstrated that the droplets have different morphologies during the process.[35] In theory, if the self-assembly of rGO and the dynamic process of partial coalescence are integrated, the shapes of the rGO aerogels could be controlled. To confirm this, a method called dynamic self-assembly (DSA) was applied to the self-assembly of SnO_2/rGO droplet aerogels, as shown in Figure 1. As the GO droplets fell from the needle tip into the target liquid (different concentrations of $SnCl_2$ solution), the GO droplets changed their shapes in a dynamic process. Because Sn^{2+} reduces GO and the reduced GO assembles to form a hydrogel, the droplet shape can be fixed. So, not only was a change in the shape of the droplets observed during the dynamic process but rGO droplet aerogels with different morphologies were obtained.

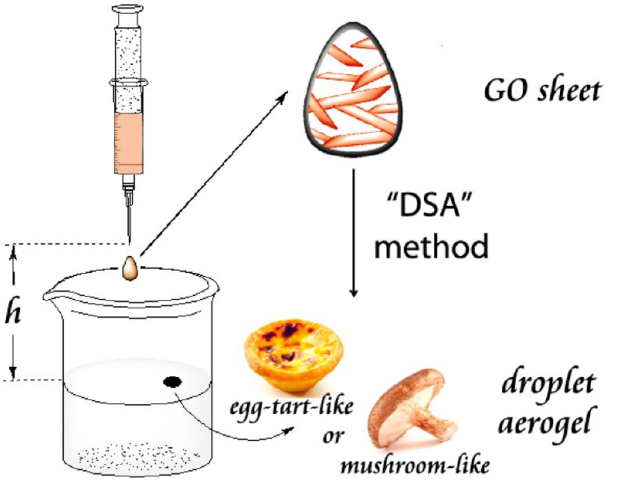

Figure 1. Schematic diagram of the DSA method.

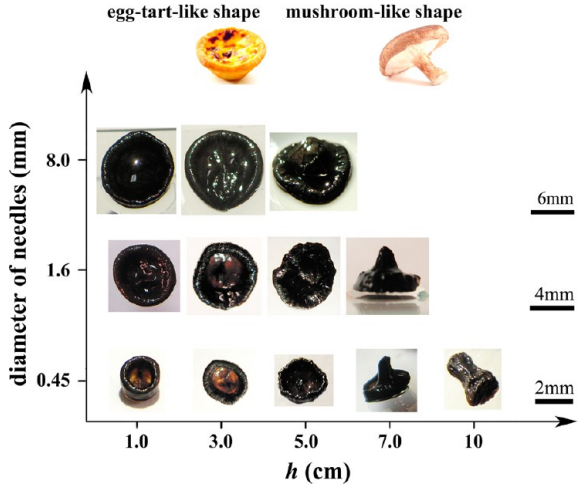

Figure 2. Effect of droplet falling height and needle diameter on the shape of SnO_2/rGO droplet aerogels.

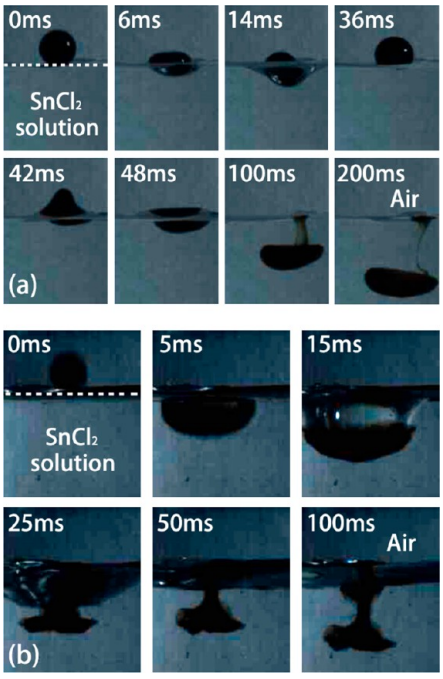

Figure 3. Formation of egg-tart-like (dropping height: 1 cm) (a) and mushroom-like (dropping height: 7 cm) and (b) SnO_2/rGO droplets observed by a high speed camera.

One of the important factors that affects the morphology of a droplet is the height (h) from which it falls. This is the distance from the tip of the needle to the surface of the target liquid (Figure 1). This height determines the instantaneous speed (v) of the droplets that strike the liquid surface and can be expressed approximately by $v = (2gh)^{1/2}$ where g is the quantity that describes the strength of gravity. This equation assumes a free falling motion and ignores any drag force from the air. Therefore, the height plays an important role in controlling the morphology of the aerogels that are formed, as shown in Figure 2. When the falling height was less than 50 mm, the speed of the drop striking the surface was 1.0 m/s, which resulted in the formation of droplets with egg-tart-like shapes. When the falling height was 70 mm (speed: 1.0−1.2 m/s), the droplets tended to be mushroom-like, and when the falling height was further increased, the morphology is difficult to control. Changing the diameter of the needle hardly changes the shape of the droplets, but their sizes changed accordingly, i.e., larger needles resulted in larger diameter. In addition, when the concentration of $SnCl_2$ solution is changed, the contents and the electrochemical properties of SnO_2 in the SnO_2/rGO droplet aerogels were altered, which will be discussed in the following paragraphs, but the morphologies have almost no change.

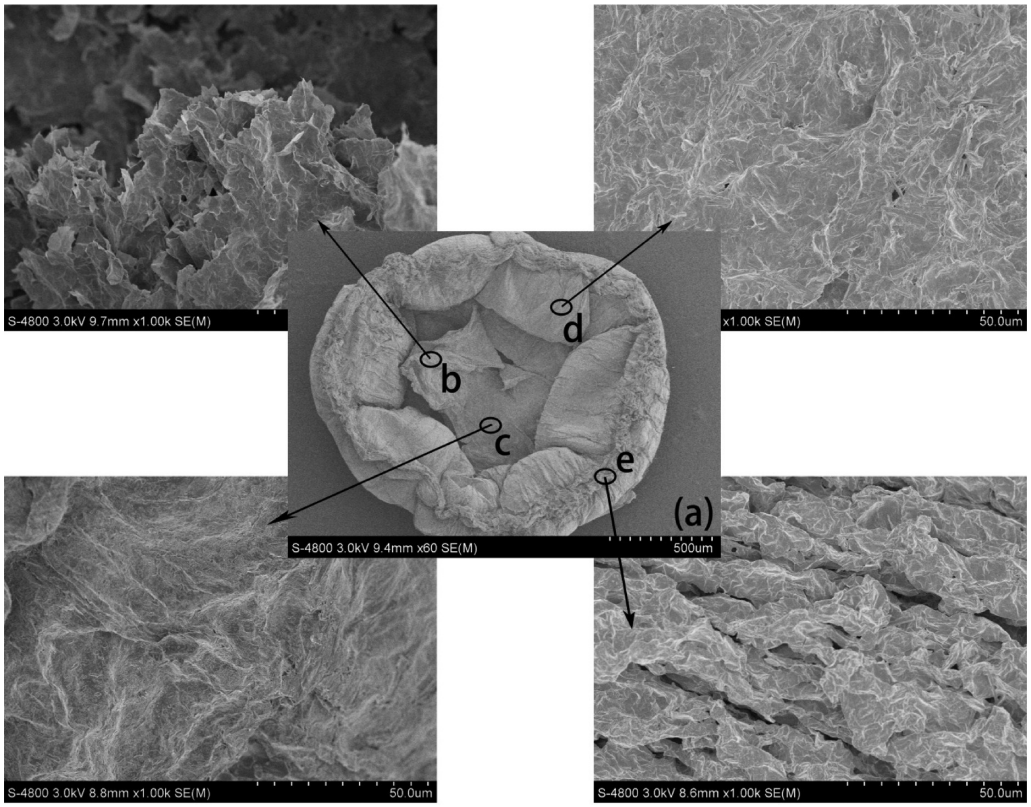

Figure 4. (a) SEM images of the egg-tart-like droplet aerogel prepared with a 0.45 mm needle and a dropping height of 1 cm; (b–e) SEM images of the different parts of egg-tart-like droplet aerogel.

To further study the changes of the droplets with time, the shapes of the droplets were recorded by a high speed camera and the results are shown in Figure 3. During the collision of the droplet with the liquid surface, most of the kinetic energy of the droplet was lost due to wave propagation and dissipation of the viscosity. The kinetic energy was fractionally converted to restorable energy, or provided the energy for the bouncing of the droplets.[36] Because the diameter of the droplet is small, the Weber number, which is is often used in analyzing fluid flows where there is an interface between two different fluids, is small at the liquid–liquid interface. The phenomenon of droplet bounce on a liquid surface usually occurs at low and moderate Weber numbers. Droplet bounce results in the possibility of generating droplets with different morphologies.[37]

When h was 1 cm, the speed of the droplets falling onto the surface was relatively slow (Figure 3a, 0 ms), so initially the GO droplet was only pairtially immersed in the liquid (Figure 3a 6 ms). The GO droplet then formed a sphere due to the surface tension (Figure 3a 14 ms) and then the droplet bounced up to the liquid surface (Figure 3a 36 ms). However, because of inertia, the upper hemisphere of the droplet continued to fall and the droplet formed a concave structure resulting in an egg-tart-like shape (Figure 3a 48, 100, and 200 ms).

In contrast, when h was 7 cm, the speed of droplets falling onto the surface was relatively fast (Figure 3b 0 ms). Therefore, as the droplet struck the surface, it became totally immersed in the water and did not maintain a spheroidal shape (Figure 3b 5 and 15 ms). The droplet bounce was more obvious and a "mushroom stem" was formed (Figure 3b 25 and 50 ms). Finally, a mushroom-like droplet formed.

The microstructure of the egg-tart-like SnO_2/rGO droplet aerogel (after freeze-drying) was observed by the SEM, and the results are shown in Figure 4. The diameter of the egg-tart is about 1.7 mm (0.45 mm diameter needle) (Figure 4a). Interestingly, the microstructure is not uniform throughout the egg-tart. A layered structure is observed around the periphery of the egg-tart (Figure 4e), which may be caused by the folding of the upper hemisphere at the moment of the droplet bounce. The other parts of the egg-tart are relatively flat (Figures 4c and 3d). However, a layerd structure can still be observed through the broken margin (Figure 4b). The microporous/mesoporous structures of SnO_2/rGO were analyzed by N_2 gas adsorption–desorption measurements, and Figure S4 (Supporting Information) exhibits a characteristic type-IV isotherm with a pronounced hysteresis in the P/P_0 range 0.4–1.0, which is a characteristic of samples with microporous structure. The well-defined micro- and mesopores are less than 20 nm mainly, and Brunauer–Emmett–Teller (BET) analysis indicated that the specific surface area of SnO_2/rGO-80 was 642.3 $m^2 \cdot g^{-1}$.

The TEM and HRTEM images of the SnO_2/rGO droplet aerogels are shown in Figure 5. In the nanometer scale, different needles get the same results. Nanoparticles are densely and uniformly loaded onto the rGO sheet (Figure 5a) and the elemental mapping of the aerogel indicated that the particles are SnO_2 (Figure 5c). On the basis of the elemental mapping of the surface and section of the SnO_2/rGO-80 droplet aerogel (Figure S5, Supporting Information), the same conclusion can be draw that SnO_2 have good dispersion on the rGO sheets. The HRTEM image (Figure 5b) shows that SnO_2 nanoparticles are smaller than 10 nm and the SnO_2 lattice interlayer spacing is 0.334 nm, which corresponds to the d-spacing of (110) SnO_2 crystal planes (The Inorganic Crystal Structure Database (ICSD), card no. 41-1445).

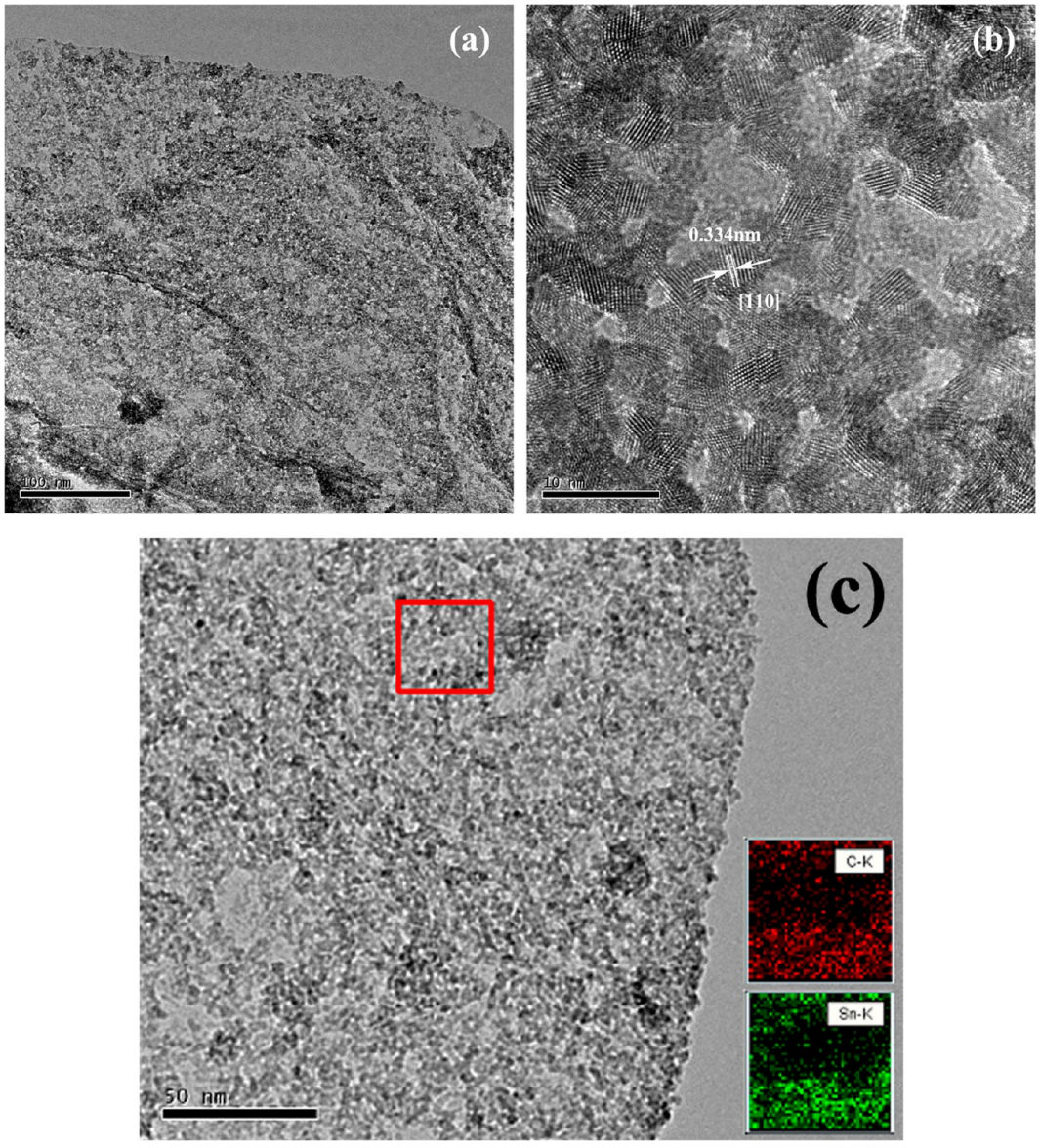

Figure 5. TEM (a, c) and HRTEM (b) images of the SnO_2/rGO-80 droplet aerogel. The inset in panel c is the STEM image and elemental mapping of the selected area of the SnO_2/rGO-80 droplet aerogel.

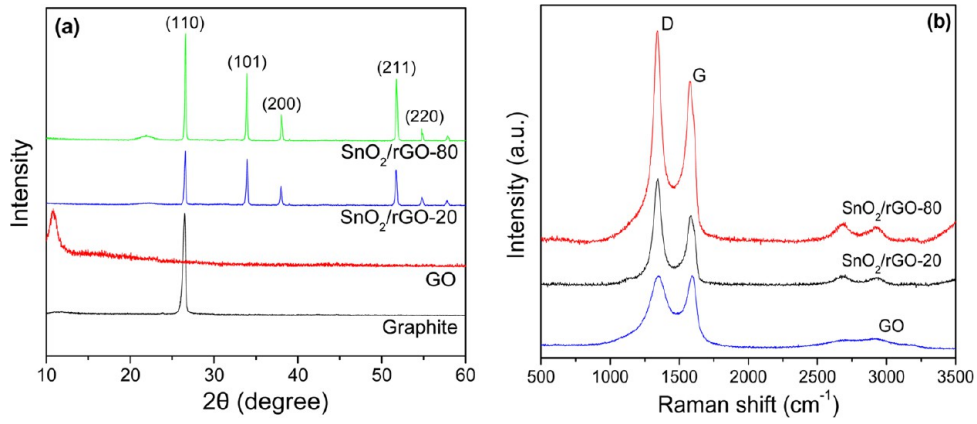

Figure 6. XRD diagrams of graphite, GO, SnO_2/rGO-20, and SnO_2/rGO-80 (a); Raman spectra of GO, SnO_2/rGO-20 and SnO_2/rGO-80 (b).

The macro- and micromorphologies that are formed in the SnO_2/rGO droplet aerogels mainly depend on the height of the falling drop. However, the shape is also determined by the redox reaction and the self-assembly of the rGO. Therefore, all

dx.doi.org/10.1021/am5036169 | ACS Appl. Mater. Interfaces 2014, 6, 14327−14337

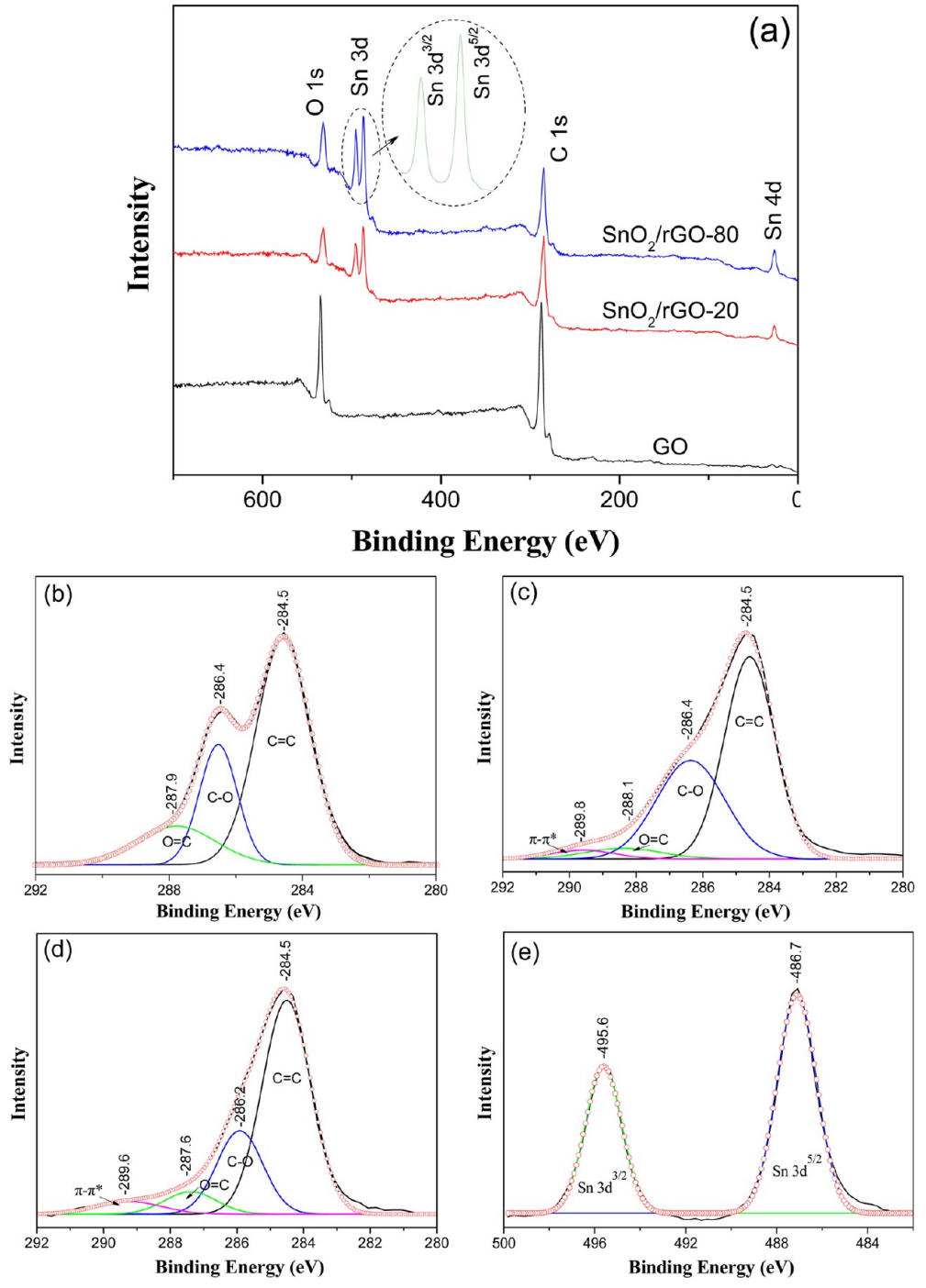

Figure 7. XPS spectra of GO, SnO_2/rGO-20, and SnO_2/rGO-80. The inset is the curve fit for the Sn_{3d} peak of SnO_2/rGO-80 (a); curve fit for C_{1s} of GO (b), SnO_2/rGO-20 (c) and SnO_2/rGO-80 (d), and curve fit for Sn_{3d} of SnO_2/rGO-80 (e).

three are key factors to the formation of SnO_2/rGO droplet aerogels by the DSA method. To better understand the transformations of GO and $SnCl_2$ during the self-assembly of the SnO_2/rGO droplet aerogel, the GO and SnO_2/rGO droplet aerogels were characterized by XRD, Raman spectroscopy, TGA, and XPS.

Figure 6a shows the XRD diagrams of graphite, GO, SnO_2/rGO-20, and SnO_2/rGO-80. GO has a characteristic peak at about 12.5°, which represents an interlayer spacing of 0.74 nm. The large interlayer spacing is due to the oxygen-containing functional groups and the intercalation of water molecules. After GO was reduced, the number of oxygen-containing functional groups decreased and the distance between layers was shortened. So, SnO_2/rGO-20 and SnO_2/rGO-80 show a weak broad peak at about 22.5°, which is between the peaks for GO and graphite (26°). The peaks located at 26.61°, 33.89°, and 51.78° in the SnO_2/rGO-20 and SnO_2/rGO-80 correspond to the tetragonal structures of SnO_2 (110), (101), and (211), respectively (ICSD, card no. 41-1445). This indicates that the Sn^{2+} transformed to SnO_2 nanocrystals during the redox reaction with GO and formed SnO_2/rGO hybrids. The standard reduction potentials explain why a redox reaction occurs between Sn^{2+} and GO. The electrode potential of GO is

Table 1. Percentage of Different Bonds in GO, SnO_2/rGO-20 and SnO_2/rGO-80

sample	analysis				
GO	carbon	oxygen	tin		C/O ratio
	75.2	24.8	0		2.9
	C=C	C—O	C=O		
	57.9	29.9	12.2		
SnO_2/rGO-20	carbon	oxygen[a]	tin	oxygen[b]	C/O ratio
	78.0	18.7	3.3	12.1	6.4
	C=C	C—O	C=O	$\pi-\pi^a$	
	65.9	25.4	5.9	2.7	
SnO_2/rGO-80	carbon	oxygen[a]	tin	oxygen[b]	C/O ratio
	71.8	21.0	7.1	6.8	10.5
	C=C	C—O	C=O	$\pi-\pi^a$	
	69.3	20.5	6.1	4.1	

[a]Oxygen in SnO_2/rGO. [b]Oxygen in rGO.

+0.48 V (relative to the standard hydrogen electrode)[38] and the standard potential for the oxidation of Sn^{2+} is given by

$$Sn^{4+} + 2e^- \rightarrow Sn^{2+},\ E^0 = 0.151\ V$$

Therefore, the redox reaction is spontaneous and the Sn^{2+} ions are oxidized to Sn^{4+} ions. Because Sn^{4+} ions are apt to hydrolyze, they transform to SnO_2 nanoparticles and then assemble on the rGO sheets.

Raman spectroscopy (Figure 6b) and TGA (Figure S1, Supporting Information) were also used to analyze the SnO_2/rGO hybrids. Generally, the Raman spectrum of graphene is characterized by two main features, the G mode arising from the first-order scattering of the E_{2g} phonons of the sp^2 C atoms (usually observed at ~1575 cm^{-1}) and the D mode due to the breathing mode of κ-point phonons with A_{1g} symmetry (at ~1350 cm^{-1}). Changes in the relative intensities of the D and G bands (D/G) are indicative of changes in the electronic conjugation state of GO. The D/G ratio increased from 0.99 for rGO to 1.20 for SnO_2/rGO-20 and 1.31 for SnO_2/rGO-80. These increases suggest that new sp^2 domains were formed and that GO was reduced during the reaction with $SnCl_2$.[39]

In the TGA diagrams, GO shows two main weight losses (Figure S1, Supporting Information). The first rapid weight loss (~15%) is at around 100 °C and can be attributed to the removal of water molecules absorbed on the GO surface. The second weight loss (~25%) between 200 and 250 °C is due to decomposition of the oxygen-containing functional groups.[34] In comparison, the weight losses of SnO_2/rGO-20 and SnO_2/rGO-80 at 230 °C were only 9.2% and 3.7%, respectively. This clearly indicates that deoxygenation was efficiently achieved by using $SnCl_2$ as a reductant. Further increasing the concentration of $SnCl_2$ solution increases the extent of the reduction.

The SnO_2/rGO droplet aerogels were also quantitatively characterized by X-ray photoelectron spectroscopy (XPS) and the results are shown in Figure 7 and Table 1. The SnO_2/rGO-20 and SnO_2/rGO-80 samples had 3.3% and 7.1% Sn, respectively. There are two peaks in the Sn 3d spectrum (Figure 7a). The one at 486.7 eV can be attributed to the Sn $3d_{5/2}$ of SnO_2 and the other at 495.6 eV can be attributed to the Sn $3d_{3/2}$ of SnO_2 (Figure 7e).[40] In the deconvoluted C 1s XPS spectrum of GO (Figure 7b), there are three peaks that can be assigned to carbon with different valences: nonoxygenated ring C (284.5 eV), the carbon in C—O bonds (286.4 eV), and carbonyl C (287.9 eV).[18] Compared to GO, the C 1s spectrum of the rGO in SnO_2/rGO (Figure 7c and 7d) have much less intense C—O and carbonyl C peaks and much larger C=C and $\pi-\pi^*$ peaks. In addition, the ratio of C/O increased from 2.9 (GO) to 6.4 and 10.5 for SnO_2/rGO-20 and SnO_2/rGO-80 respectively (these numbers were calculated after the oxygen from the SnO_2 was deducted from the total oxygen in the SnO_2/rGO). These results imply that the oxygen-functional groups were eliminated, the sp^2 domains were re-established and that the GO were reduced.

A control experiment was done to determine the role of the GO/$SnCl_2$ redox reaction in the DSA method, and the result of the control experiment is shown in Figure 8. When the GO droplet fell into the pure water or the other salt solutions, because of the similar stress situation, the special shape of the GO droplet was able to form in a short moment, but soon, the droplet scattered into plenty of small irregular precipitates. Comparatively, other things being equal except adding $SnCl_2$ into the water, because the GO droplet was reduced fast in the $SnCl_2$ solution at room temperature, the special shape was able to be maintained. Therefore, both the dynamic process and the reduction play important roles in the DSA method.

3.2. Electrochemical Capacitive Performance of the SnO_2/rGO Aerogel in a Two-Electrode Supercapacitor Cell. A major issue that is commonly faced in the testing of the performance of supercapacitors is that comparisons of various electrode materials are difficult because different electrode assemblies are often used. In two-electrode configurations, two active electrodes (one positive and one negative) are separated by a porous matrix (a separator) and immersed in an electrolyte for analysis. In contrast, in a three electrode system, one active electrode is used for analysis in the presence of a counter and reference electrode. Theoretically, three electrode system gives four times higher capacitance value than two-electrode system, but the three electrode system does not represent a real situation and cannot be used for practical applications. Therefore, in this work, a two-electrode cell configuration was used. Even though the two-electrode measurement method gives a lower capacitance value, it is a more realistic value.[41]

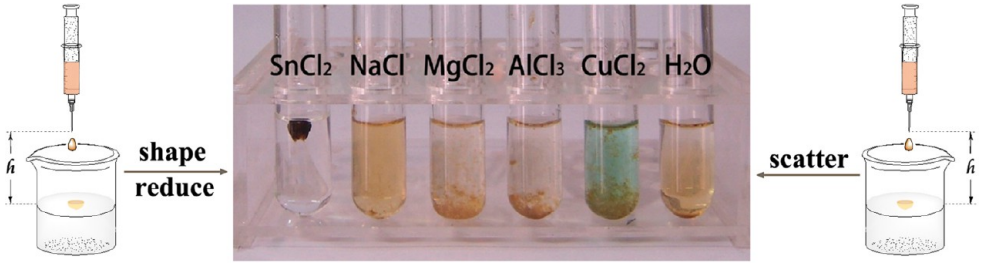

Figure 8. Photograph of the GO droplet falling into pure water and different salt solutions.

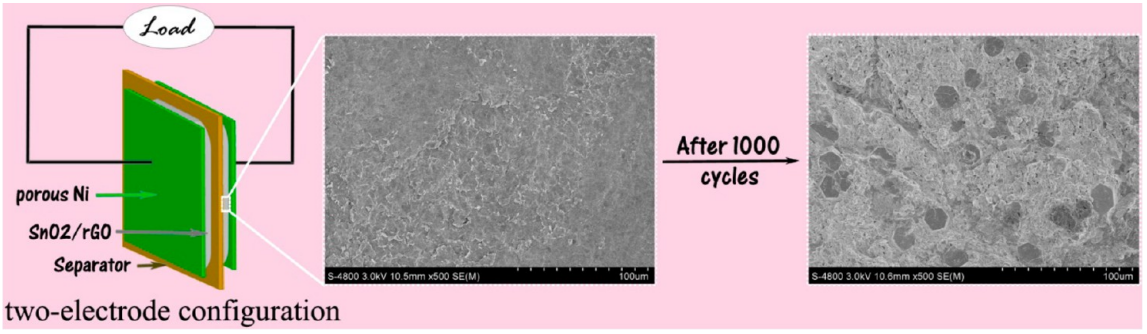

Figure 9. Schematic illustration of a two-electrode supercapacitor device and SEM images of the electrode material.

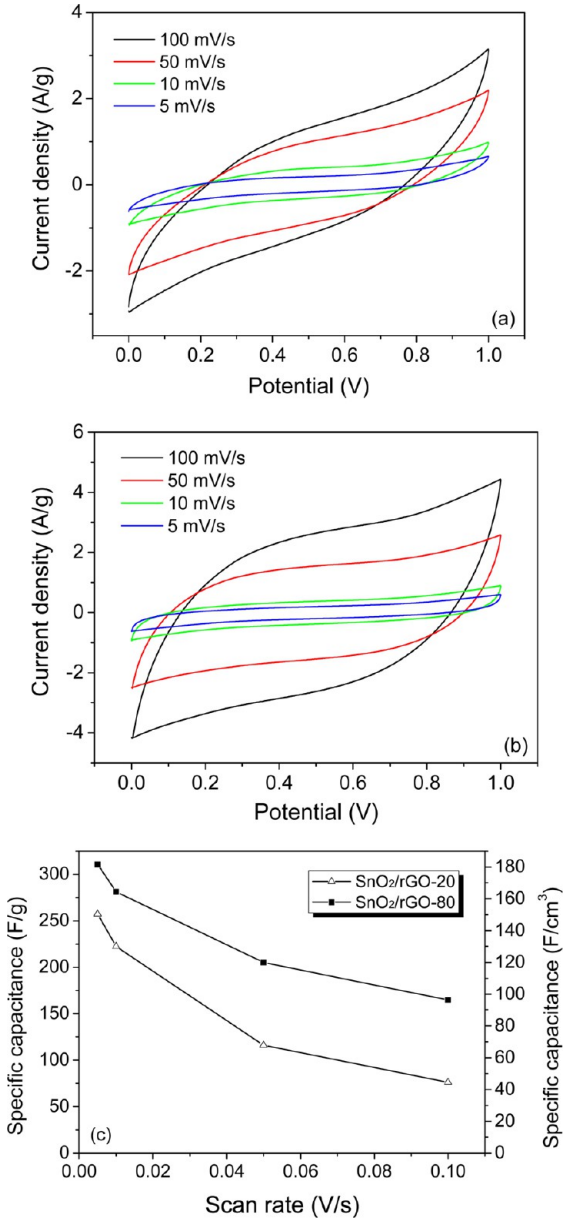

Figure 10. CV curves of SnO_2/rGO-20 (a) and SnO_2/rGO-80 (b) at various scan rates in 2 M KOH solution and the gravimetric and volumetric specific capacitances at various scan rates (c).

A symmetrical supercapacitor device was fabricated using the same method that is used in industry (see the Experimenal Section), and a schematic for the device is shown in Figure 9. The symmetrical supercapacitor was used to evaluate the electrochemical activity of the SnO_2/rGO electrodes.

Figure 10 shows the cyclic voltammetry (CV) curves of the SnO_2/rGO-20 and SnO_2/rGO-80 electrodes in 2 M KOH aqueous solution. The CV profiles were obtained from 0 to 1 V at different scan rates (from 5 to 100 mV·s^{-1}). The CV curves are nearly rectangular in shape, indicating that the electrodes have a near-ideal capacitive behavior.[42] The shapes at high scan rates are similar to those at low scan rates with no obvious distortion, indicating a high rate performance and excellent ionic and electronic transport within the electrode material.[43]

The specific capacitances (SCs) based on the masses and volumes of the SnO_2/rGO-20 and SnO_2/rGO-80 electrodes are shown in Figure 10c. At a scan rate of 5 mV/s, the gravimetric and volumetric SCs for SnO_2/rGO-20 are 257 F/g and 149 F/cm^3, respectively, and those for SnO_2/rGO-80 are 310 F/g and 180 F/cm^3, respectively. The SC values decreased with scan rate, which can be attributed to the fact that at high scan rates the electrolyte ions are unable to fully access the interior surfaces of the active materials. This is due to reduced diffusion times at higher scan rates.[44] Meanwhile, because of the loading of SnO_2 improving, the SCs of supercapacitor increased. In addition, the SC values of the SnO_2/rGO electrodes are similar to those for MnO_2 nanowire/graphene,[45] and are higher than that of the pure rGO (Figure S2, Supporting Information).

The triangular-shape galvanostatic charge/discharge curves of the SnO_2/rGO-20 and SnO_2/rGO-80 electrodes measured at different current densities are shown in Figures 11a and 10b, respectively. The specific capacitances of SnO_2/rGO-20 and SnO_2/rGO-80 were calculated from these curves. At a current density the of 0.5 A/g, the gravimetric and volumetric SCs are 231 F/g and 113 F/cm^3 for SnO_2/rGO-80, respectively, and 179 F/g and 103 F/cm^3 for SnO_2/rGO-20, respectively (Figure 11c). Again, the SnO_2/rGO-80 electrode, which supports more SnO_2 nanoparticles, has a higher capacitance and the SC values of all the SnO_2/rGO electrodes were higher than that of the pure rGO (Figure S2, Supporting Information). These results demonstrate that the SnO_2 nanoparticles improve the SC value.

In Figure 11d, the Nyquist plot of the SnO_2/rGO-20 and SnO_2/rGO-80 electrodes shows a straight line in the low-frequency region and an arc in the high frequency region. The inconspicuous arc in the high frequency region indicates that the electronic resistances of SnO_2/rGO-20 and SnO_2/rGO-80 are low. The slope of the 45° portion of the curve is called the Warburg resistance and is a result of the frequency dependence of the ion diffusion of the electrolyte to the electrode interface.[41] The equivalent series resistance (ESR) of SnO_2/rGO-20 and SnO_2/rGO-80 were obtained from the curve fitted to the Nyquist plot and were determined to be 0.7 and 0.6 Ω,

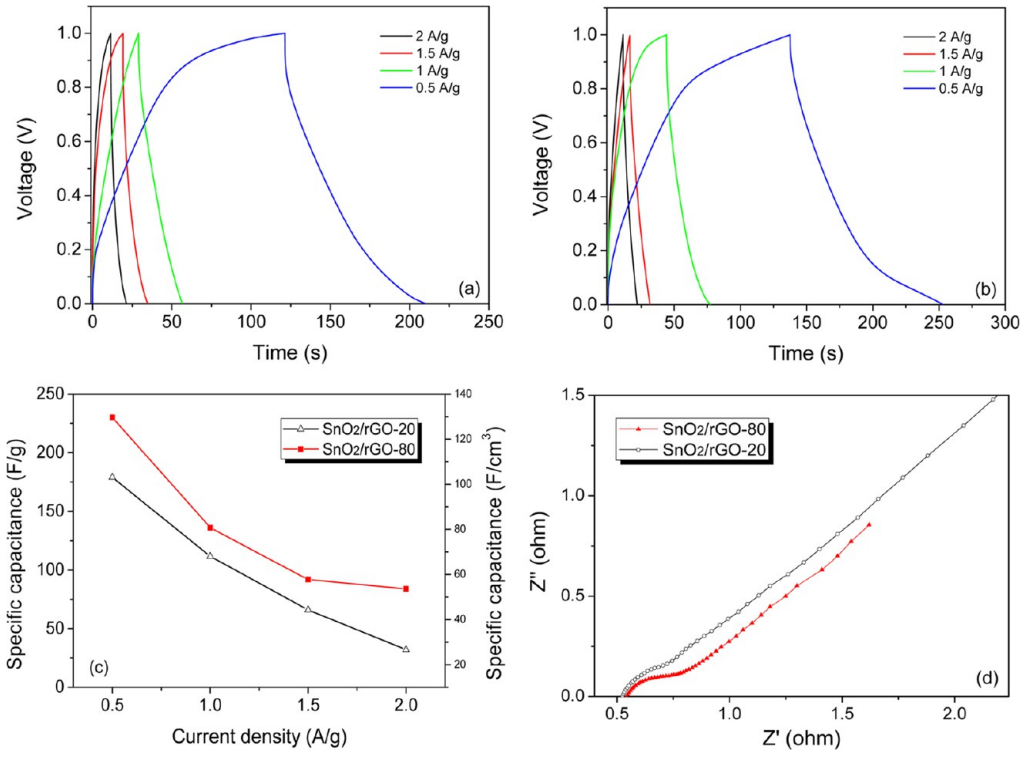

Figure 11. Galvanostatic charge/discharge curves for SnO_2/rGO-20 (a) and SnO_2/rGO-80 (b) under different current densities in 2 M KOH solution; gravimetric and volumetric specific capacitances under different current densities (c) and the electrochemical impedance spectraof SnO_2/rGO-20 and SnO_2/rGO-80 symmetric electrodes in the frequency range of 100 kHz to 0.1 Hz (d).

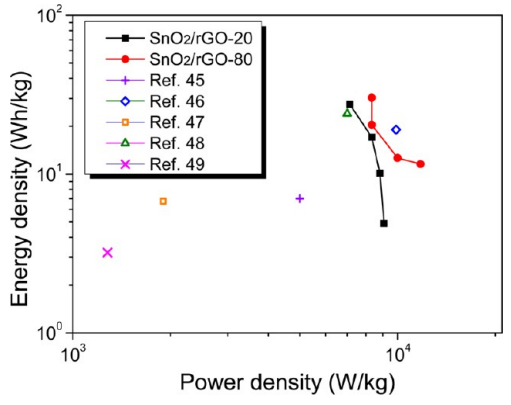

Figure 12. Energy and power densities for SnO_2/rGO-20 and SnO_2/rGO-80 in 2 M KOH solution under different current densities.[45−49]

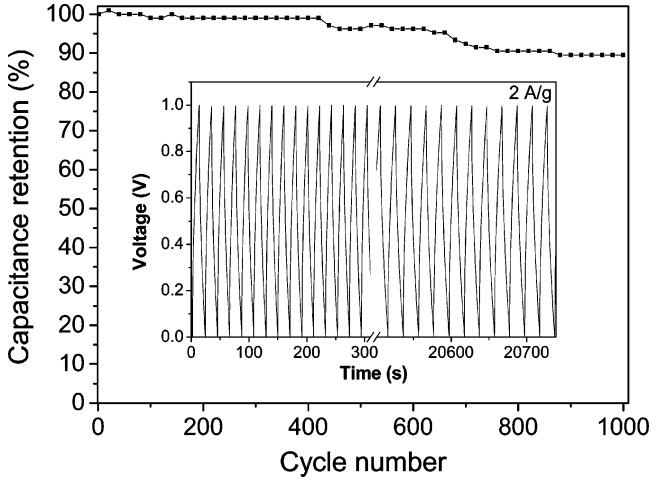

Figure 13. Capacitance retention of SnO_2/rGO-80 in 2 M KOH solution at a constant current density of 2 A/g. The inset shows the charge−discharge curves of the SnO_2/rGO-80.

respectively. The ESR is related to the rate that a supercapacitor can be charged and discharged, and it is also related to the maximum power density of a supercapacitor.

The energy and power densities of the capacitors were calculated from the charge−discharge results and these are summarized as a Ragone plot in Figure 12. The energy and power densities for SnO_2/rGO-80 are slightly better than those for SnO_2/rGO-20. The energy density of SnO_2/rGO-80 was 30 $Wh{\cdot}kg^{-1}$ at a power density of 8.3 $kW{\cdot}kg^{-1}$ and it decreased as the power density was increased. At a high power density of 11.8 $kW{\cdot}kg^{-1}$, the energy density was still 11.6 $Wh{\cdot}kg^{-1}$. Notably the energy density is higher than those of graphene/SnO_2/polypyrrole[46] and MnO_2 nanowire/graphene.[45] The maximum power density of SnO_2/rGO-80 was 20 $kW{\cdot}kg^{-1}$. It is reported that the removal of inactive materials, such as binders and conductive agents, can greatly increases the specific energy density.[50] In this work, the aerogel can used as an electrode directly without binder and carbon black, which helps improve the supercapacitor performs of the material.

To study the usefulness of SnO_2/rGO-80 as a supercapacitor, the capacitance retention was measured for 1000 charge/discharge cycles at a current density of 2 A/g, and the results are shown in Figure 13. After 1000 charge/discharge cycles, the SnO_2/rGO-80 electrode retained about 90% of its initial capacitance, indicating good cycle-life stability. Capacity loss with extended cycling is a common phenomenon in supercapacitors and speculated that it is related with the macrospores of graphene after 1000 charge/discharge cycles (Figure 9).

dx.doi.org/10.1021/am5036169 | ACS Appl. Mater. Interfaces 2014, 6, 14327−14337

However, the slight decay in the SC can be ascribed to the fact that the rGO inhibits aggregation of the SnO_2 nanoparticles, which can observe clearly in Figure S6 (Supporting Information). This stable cycle performance indicates that the SnO_2/rGO-80 electrode is highly durable for electrochemical capacitor applications in mild aqueous electrolytes.

4. CONCLUSIONS

A novel and facile method, DSA, has been developed for controlling and observing the morphology of SnO_2/rGO aerogels. The method combines a redox reaction, the self-assembly of rGO, and the dynamic process of a drop falling into a target solution. As the falling GO droplets struck the target $SnCl_2$ solution, the shape of the GO droplets changed. Because Sn^{2+} reduces GO and the reduced GO self-assembles to form an aerogel, the droplet shape can be solidified. So, not only can the changes in the shape of the droplets be observed during the dynamic process, but SnO_2/rGO droplet aerogels with different morphologies, including egg-tart and mushroom shapes can also be obtained. The SnO_2/rGO aerogels were used as electrode materials in supercapacitors and showed excellent electrochemical performance with good energy storage and good stability.

■ ASSOCIATED CONTENT

Supporting Information

TGA curves, CV curves and Galvanostatic charge/discharge curves of GO, SnO_2/rGO-20 and SnO_2/rGO-80, N_2 sorption isotherms, SEM images and HRTEM image of SnO_2/rGO-80. This material is available free of charge via the Internet at http://pubs.acs.org.

■ AUTHOR INFORMATION

Corresponding Authors

*J. P. Gao. Tel.: +8615522461762. Fax: (+86)22-2740-3475. E-mail: jianpinggaols@126.com.
*Y. Liu. E-mail: liuyuls@163.com.

Notes

The authors declare no competing financial interest.

■ ACKNOWLEDGMENTS

Funding from the National Natural Science Foundation of China (21202115, 21276181, and 21074089) is gratefully acknowledged.

■ REFERENCES

(1) Wang, H.; Rogach, A. L. Hierarchical SnO_2 Nanostructures: Recent Advances in Design, Synthesis, and Applications. *Chem. Mater.* **2014**, *26*, 123−133.
(2) Han, X.; Jin, M.; Xie, S.; Kuang, Q.; Jiang, Z.; Jiang, Y.; Xie, Z.; Zheng, L. Synthesis of Tin Dioxide Octahedral Nanoparticles with Exposed High-Energy {221} Facets and Enhanced Gas-Sensing Properties. *Angew. Chem., Int. Ed.* **2009**, *48*, 9180−9183.
(3) Wang, C.; Zhou, Y.; Ge, M.; Xu, X.; Zhang, Z.; Jiang, J. Z. Large-Scale Synthesis of SnO_2 Nanosheets with High Lithium Storage Capacity. *J. Am. Chem. Soc.* **2009**, *132*, 46−47.
(4) Xu, X.; Zhuang, J.; Wang, X. SnO_2 Quantum Dots and Quantum Wires: Controllable Synthesis, Self-Assembled 2D Architectures, and Gas-Sensing Properties. *J. Am. Chem. Soc.* **2008**, *130*, 12527−12535.
(5) Prasittichai, C.; Hupp, J. T. Surface Modification of SnO_2 Photoelectrodes in Dye-sensitized Solar Cells: Significant Improvements in Photovoltage via Al_2O_3 Atomic Layer Deposition. *J. Phys. Chem. Lett.* **2010**, *1*, 1611−1615.
(6) Zhang, H.; Hu, C. Effective Solar Absorption and Radial Microchannels of SnO_2 Hierarchical Structure for High Photocatalytic Activity. *Catal. Commun.* **2011**, *14*, 32−36.
(7) Hassan, F. M.; Chen, Z. W.; Yu, A. P.; Chen, Z.; Xiao, X. C. Sn/SnO_2 Embedded in Mesoporous Carbon Nanocomposites as Negative Electrode for Lithium Ion Batteries. *Electrochim. Acta* **2013**, *87*, 844−852.
(8) Liu, Y.; Jiao, Y.; Zhang, Z.; Qu, F.; Umar, A.; Wu, X. Hierarchical SnO_2 Nanostructures Made of Intermingled Ultrathin Nanosheets for Environmental Remediation, Smart Gas Sensor, and Supercapacitor Applications. *ACS Appl. Mater. Interfaces* **2014**, *6*, 2174−2184.
(9) Wang, S.; Jiang, S. P.; Wang, X. Microwave-Assisted One-Pot Synthesis of Metal/Metal Oxide Nanoparticles on Graphene and Their Electrochemical Applications. *Electrochim. Acta* **2011**, *56*, 3338−3344.
(10) Novoselov, K. S.; Geim, A. K.; Morozov, S. V.; Jiang, D.; Zhang, Y.; Dubonos, S. V.; Grigorieva, I. V.; Firsov, A. A. Electric Field Effect in Atomically Thin Carbon Films. *Science* **2004**, *306*, 666−669.
(11) Geim, A. K.; Novoselov, K. S. The Rise of Graphene. *Nat. Mater.* **2007**, *6*, 183−191.
(12) Dreyer, D. R.; Park, S.; Bielawski, C. W.; Ruoff, R. S. The Chemistry of Graphene Oxide. *Chem. Soc. Rev.* **2010**, *39*, 228−240.
(13) James, D. K.; Tour, J. M. Graphene: Powder, Flakes, Ribbons, and Sheets. *Acc. Chem. Res.* **2013**, *46*, 2307−2318.
(14) Lightcap, I. V.; Kamat, P. V. Graphitic Design: Prospects of Graphene-based Nanocomposites for Solar Energy Conversion, Storage, and Sensing. *Acc. Chem. Res.* **2013**, *46*, 2235−2243.
(15) Kim, K. S.; Zhao, Y.; Jang, H.; Lee, S. Y.; Kim, J. M.; Kim, K. S.; Ahn, J. H.; Kim, P.; Choi, J. Y.; Hong, B. H. Large-Scale Pattern Growth of Graphene Films for Stretchable Transparent Electrodes. *Nature* **2009**, *457*, 706−710.
(16) Berger, C.; Song, Z.; Li, X.; Wu, X.; Brown, N.; Naud, C.; Mayou, D.; Li, T.; Hass, J.; Marchenkov, A. N.; Conrad, E. H.; First, P. N.; Heer, W. A. Electronic Confinement and Coherence in Patterned Epitaxial Graphene. *Science* **2006**, *312*, 1191−1196.
(17) Chua, C. K.; Pumera, M. Chemical Reduction of Graphene Oxide: A Synthetic Chemistry Viewpoint. *Chem. Soc. Rev.* **2014**, *43*, 291−312.
(18) Seo, M.; Yoon, D.; Hwang, K. S.; Kang, J. W.; Kim, J. Supercritical Alcohols as Solvents and Reducing Agents for the Synthesis of Reduced Graphene Oxide. *Carbon* **2013**, *64*, 207−218.
(19) Huang, C.; Li, C.; Shi, G. Graphene based Catalysts. *Energy Environ. Sci.* **2012**, *5*, 8848−8868.
(20) Zeng, Q.; Cheng, J.; Tang, L.; Liu, X.; Liu, Y.; Li, J.; Jiang, J. Self-Assembled Graphene-Enzyme Hierarchical Nanostructures for Electrochemical Biosensing. *Adv. Funct. Mater.* **2010**, *20*, 3366−3372.
(21) Cui, X.; Wu, S.; Jungwirth, S.; Chen, Z.; Wang, Z.; Wang, L.; Li, Y. The Deposition of Au−Pt Core−Shell Nanoparticles on Reduced Graphene Oxide and Their Catalytic Activity. *Nanotechnology* **2013**, *24*, 295402.
(22) Tan, C.; Huang, X.; Zhang, H. Synthesis and Applications of Graphene-based Noble Metal Nanostructures. *Mater. Today* **2013**, *16*, 29−36.
(23) Chen, M.; Zhang, C.; Li, X.; Zhang, L.; Ma, Y.; Zhang, L.; Ma, Y.; Zhang, L.; Xu, X.; Xia, F.; Wang, W.; Gao, J. A One-Step Method for Reduction and Self-Assembling of Graphene Oxide into Reduced Graphene Oxide Aerogels. *J. Mater. Chem. A* **2013**, *1*, 2869−2877.
(24) Ji, C. C.; Xu, M. W.; Bao, S. J.; Cai, C. J.; Lu, Z. J.; Chai, H.; Yang, F.; Hua, W. Self-Assembly of Three-Dimensional Interconnected Graphene-based Aerogels and Its Application in Supercapacitors. *J. Colloid Interface Sci.* **2013**, *407*, 416−424.
(25) Worsley, M. A.; Pauzauskie, P. J.; Olson, T. Y.; Biener, J.; Satcher, J. H.; Baumann, T. F. Synthesis of Graphene Aerogel with High Electrical Conductivity. *J. Am. Chem. Soc.* **2010**, *132*, 14067−14069.
(26) Nardecchia, S.; Carriazo, D.; Ferrer, M. L.; Gutiérrez, M. C.; Monte, F. Three Dimensional Macroporous Architectures and Aerogels Built of Carbon Nanotubes and/or Graphene: Synthesis and Applications. *Chem. Soc. Rev.* **2013**, *42*, 794−830.

(27) Ye, S. B.; Feng, J. C.; Wu, P. Y. Deposition of Three-Dimensional Graphene Aerogel on Nickel Foam as a Binder-free Supercapacitor Electrode. *ACS. Appl. Mater. Interfaces* **2013**, *5*, 7122−7129.
(28) Blanchette, F.; Messio, L.; Bush, J. W. M. The Influence of Surface Tension Gradients on Drop Coalescence. *Phys. Fluids* **2009**, *21*, 072107.
(29) Capretto, L.; Mazzitelli, S.; Balestra, C.; Tosib, A.; Nastruzzi, C. Effect of the Gelation Process on the Production of Alginate Microbeads by Microfluidic Chip Technology. *Lab Chip* **2008**, *8*, 617−621.
(30) Fedorchenko, A. I.; Wang, A. On Some Common Features of Drop Impact on Liquid Surfaces. *Phys. Fluids* **2004**, *16*, 1349−1365.
(31) Mele, E.; Fragouli, D.; Ruffilli, R.; Gregorio, G. L.; Cingolanid, R.; Athanassioua, A. Complex Architectures Formed by Alginate drops Floating on Liquid Surfaces. *Soft Matter* **2013**, *9*, 6338−6343.
(32) Charles, G. E.; Mason, S. G. The Mechanism of Partial Coalescence of Liquid Drops at Liquid/Liquid Interfaces. *J. Colloid Sci.* **1960**, *15*, 105−122.
(33) Klyuzhin, I. S.; Ienna, F.; Roeder, B.; Wexler, A.; Pollack, G. H. Persisting Water Droplets on Water Surfaces. *J. Phys. Chem. B* **2010**, *114*, 14020−14027.
(34) Chen, M.; Zhang, C.; Li, L.; Liu, Y.; Li, X.; Xu, X.; Xia, F.; Wang, W.; Gao, J. Sn Powder as Reducing Agents and SnO_2 Precursors for the Synthesis of SnO_2-Reduced Graphene Oxide Hybrid Nanoparticles. *ACS Appl. Mater. Interfaces* **2013**, *5*, 13333−13339.
(35) Zou, J.; Ren, Y.; Ji, C.; Ruan, X.; Fu, X. Phenomena of a Drop Impact on a Restricted Liquid Surface. *Exp. Therm. Fluid Sci.* **2013**, *51*, 332−341.
(36) Chen, X.; Mandre, S.; Feng, J. J. An Experimental Study of the Coalescence between a Drop and an Interface in Newtonian and Polymeric Liquids. *Phys. Fluids* **2006**, *18*, 092103.
(37) Zou, J.; Wang, P. F.; Zhang, T. R.; Fu, X.; Ruan, X. Experimental Study of a Drop Bouncing on a Liquid Surface. *Phys. Fluids* **2011**, *23*, 044101.
(38) Chen, X.; Wu, G.; Chen, J.; Chen, X.; Xie, Z.; Wang, X. Synthesis of "Clean" and Well-Dispersive Pd Nanoparticles with Excellent Electrocatalytic Property on Graphene Oxide. *J. Am. Chem. Soc.* **2011**, *133*, 3693−3695.
(39) Desiraju, G. R. Hydrogen Bridges in Crystal Engineering: Interactions without Borders. *Acc. Chem. Res.* **2002**, *35*, 565−573.
(40) Grutsch, P. A.; Zeller, M. V.; Fehlner, T. P. Photoelectron Spectroscopy of Tin Compounds. *Inorg. Chem.* **1973**, *12*, 1431−1433.
(41) Bhattacharjya, D.; Kim, M. S.; Bae, T. S.; Yu, J. S. High Performance Supercapacitor Prepared from Hollow Mesoporous Carbon Capsules with Hierarchical Nanoarchitecture. *J. Power Sources* **2013**, *244*, 799−805.
(42) Zhang, K.; Zhang, L. L.; Zhao, X. S.; Wu, J. S. Graphene/Polyaniline Nanofiber Composites as Supercapacitor Electrodes. *Chem. Mater.* **2010**, *22*, 1392−1401.
(43) Biswas, S.; Drzal, L. T. Multilayered Nanoarchitecture of Graphene Nanosheets and Polypyrrole Nanowires for High Performance Supercapacitor Electrodes. *Chem. Mater.* **2010**, *22*, 5667−5671.
(44) Wang, J. G.; Yang, Y.; Huang, Z. H.; Kang, F. Y. Rational Synthesis of MnO_2/Conducting Polypyrrole@Carbon Nanofiber Triaxial Nano-Cables for High-Performance Supercapacitors. *J. Mater. Chem.* **2012**, *22*, 16943−16949.
(45) Wu, Z. S.; Ren, W.; Wang, D. W.; Li, F.; Liu, B.; Cheng, H. M. High-Energy MnO_2 Nanowire/Graphene and Graphene Asymmetric Electrochemical Capacitors. *ACS Nano* **2010**, *4*, 5835−5842.
(46) Wang, W.; Hao, Q.; Lei, W.; Xia, X.; Wang, X. Graphene/SnO_2/Polypyrrole Ternary Nanocomposites as Supercapacitor Electrode Materials. *RSC Adv.* **2012**, *2*, 10268−10274.
(47) Le, L. T.; Ervin, M. H.; Qiu, H.; Fuchs, B. E.; Lee, W. Y. Graphene Supercapacitor Electrodes Fabricated by Inkjet Printing and Thermal Reduction of Graphene Oxide. *Electrochem. Commun.* **2011**, *13*, 355−358.
(48) Cheng, Y.; Zhang, H.; Lu, S.; Varanasiad, C. V.; Liu, J. Flexible Asymmetric Supercapacitors with High Energy and High Power Density in Aqueous Electrolytes. *Nanoscale* **2013**, *5*, 1067−1073.
(49) Cheng, Y.; Lu, S.; Zhang, H.; Varanasi, C. V.; Liu, J. Synergistic Effects from Graphene and Carbon Nanotubes Enable Flexible and Robust Electrodes for High-Performance Supercapacitors. *Nano Lett.* **2012**, *12*, 4206−4211.
(50) Zhou, G.; Li, F.; Cheng, H. Progress in Flexible Lithium Batteries and Future Prospects. *Energy Environ. Sci.* **2014**, *7*, 1307−1338.